Journal of Zhejiang University-SCIENCE A (Applied Physics & Engineering) 2025 26(3):238-251
www.jzus.zju.edu.cn; www.springer.com/journal/11582
E-mail: jzus_a@zju.edu.cn

Research Article

https://doi.org/10.1631/jzus.A2300641

Numerical simulation of 3D supersonic asymmetric truncated nozzle based on *k-kL* algebraic stress model

Gang WANG, Shuai ZHANG, Jifa ZHANG✉, Yao ZHENG

School of Aeronautics and Astronautics, Zhejiang University, Hangzhou 310027, China

Abstract: The nozzle is a critical component responsible for generating most of the net thrust in a scramjet engine. The quality of its design directly affects the performance of the entire propulsion system. However, most turbulence models struggle to make accurate predictions for subsonic and supersonic flows in nozzles. In this study, we explored a novel model, the algebraic stress model *k-kL*-ARSM+J, to enhance the accuracy of turbulence numerical simulations. This new model was used to conduct numerical simulations of the design and off-design performance of a 3D supersonic asymmetric truncated nozzle designed in our laboratory, with the aim of providing a realistic pattern of changes. The research indicates that, compared to linear eddy viscosity turbulence models such as *k-kL* and shear stress transport (SST), the *k-kL*-ARSM+J algebraic stress model shows better accuracy in predicting the performance of supersonic nozzles. Its predictions were identical to the experimental values, enabling precise calculations of the nozzle. The performance trends of the nozzle are as follows: as the inlet Mach number increases, both thrust and pitching moment increase, but the rate of increase slows down. Lift peaks near the design Mach number and then rapidly decreases. With increasing inlet pressure, the nozzle thrust, lift, and pitching moment all show linear growth. As the flight altitude rises, the internal flow field within the nozzle remains relatively consistent due to the same supersonic nozzle inlet flow conditions. However, external to the nozzle, the change in external flow pressure results in the nozzle exit transitioning from over-expanded to under-expanded, leading to a shear layer behind the nozzle that initially converges towards the nozzle center and then diverges.

Key words: Supersonic nozzle; Turbulence model; Numerical simulation; Performance analysis

1 Introduction

With the rapid development of hypersonic technology, air-breathing hypersonic propulsion systems have attracted increasing attention from researchers (Lv et al., 2017; Liao et al., 2018; Wen et al., 2019). Air-breathing hypersonic propulsion systems do not require oxidizers to be carried and can provide a higher specific impulse, making them a more suitable power solution for hypersonic aircraft than rocket propulsion systems (Edwards et al., 1975). In air-breathing hypersonic propulsion systems, the nozzle plays a critical role in producing most of the thrust, and its design significantly affects the overall performance of the propulsion system. Studies have shown that when cruising at speeds near Mach 6 (*Ma*=6), the nozzle contributes about 70% of the total thrust generated by the entire propulsion system (Edwards et al., 1975). A mere 1% reduction in the nozzle thrust coefficient can result in about a 4% decrease in the overall thrust performance of the entire propulsion system (Lederer and Krüger, 1993). Hence, achieving a highly efficient and high-performance engine necessitates meticulous design considerations for the nozzle. Given the design demands for integrated airframe and propulsion (Zhang et al., 2019; Zheng et al., 2019; Yu and Wei, 2023), the single expansion ramp nozzle (SERN) has emerged as the most widely used nozzle configuration (Li et al., 2021). The SERN uses the aft body of the aircraft as an extension of the expansion surface, accelerating high-temperature and high-pressure gases to generate most of the thrust. This approach reduces the weight of the airframe and decreases the frictional drag. Furthermore, the SERN shows good adaptability under off-design conditions and can achieve favorable

✉ Jifa ZHANG, jfzhang@zju.edu.cn
Gang WANG, https://orcid.org/0000-0002-0452-7286

Received Dec. 19, 2023; Revision accepted Mar. 18, 2024;
Crosschecked Feb. 10, 2025

aerodynamic performance (Nickerson et al., 1988; Herrmann and Rick, 1991).

Extensive research has been conducted on single expansion ramp nozzles, leading to the formulation of various design approaches, including methods for achieving maximum thrust and minimizing length (Nickerson et al., 1988; Göing, 1990; Baysal, 1992). Yu et al. (2020) proposed a nozzle inverse design method based on the maximum thrust theory and the method of characteristic (MOC). This method, compared to typical maximum thrust nozzle design approaches, not only leverages the maximum thrust theory but also offers greater flexibility under geometric constraints. Miao et al. (2023) proposed an over-under turbine-based combined cycle engine (TBCC) nozzle design method optimized for thrust under given geometric constraints, focusing on the strong coupling between the wide-speed-range aircraft body and propulsion. Extensive numerical and experimental research has also been conducted to obtain detailed performance characteristics of such nozzles. Koschel and Rick (1991) used numerical methods to compare the performance of SERN-type nozzles and plug nozzles. The computational results indicate that, under hypersonic flight conditions, 2D SERN nozzles can achieve similar performance to plug nozzles. However, at lower flight states, particularly during transonic flight, the axial thrust coefficient significantly decreases. Gruhn et al. (2000, 2002) investigated the flow at the SERN ramp region using numerical and experimental methods. Their research suggested that optimizing the contour of the ramp could be used to enhance the axial thrust of the nozzle. Hirschen et al. (2008, 2009) and Hirschen and Gülhan (2009) conducted experimental research on SERN in a hypersonic wind tunnel with a free-stream Mach number of Ma=7. The study revealed that the flow characteristics of a single expansion ramp nozzle are significantly influenced by its geometric shape. The internal flow within the nozzle is greatly affected by the nozzle's geometry, and the interaction between the internal and external flows depends on the nozzle pressure ratio and free-stream Reynolds number. Therefore, during the early design phase, nozzles should be designed to operate as closely as possible to their intended working range.

Research on 3D nozzles holds significant importance in advancing air-breathing hypersonic aircraft technology. In our laboratory, a 3D supersonic asymmetric truncated nozzle was designed based on the MOC and streamlined tracing techniques (Billig and Kothari, 2000). To achieve the appropriate length, nonlinear truncation techniques (Quan et al., 2012) were used in the nozzle compression process. Using orthogonal design and Kriging surrogate models, a multi-objective optimization design (Zhu et al., 2018) was executed, focusing on thrust and lift as the key objectives. The application of computational fluid dynamics (CFD) and multi-objective design (MOD) techniques in the conceptual design phase significantly improved both the efficiency and accuracy of the nozzle design. Due to the asymmetry of the single expansion ramp nozzle in the pitching direction, variation in the thrust and thrust vector under different conditions has a significant impact on the aircraft. Therefore, the study of off-design conditions for the nozzle is of great importance.

With the advancement of numerical simulation techniques, numerical computation has become an indispensable tool in research. Currently, the main numerical simulation methods for studying flow phenomena include direct numerical simulation (DNS), large eddy simulation (LES), and Reynolds-averaged Navier-Stokes (RANS) equations (Wang et al., 2021). Although DNS and LES are capable of accurately capturing fine details of real flow fields, these methods are impractical for engineering applications due to the extensive computational grids they demand. Therefore, RANS remains the preferred numerical simulation method for complex geometries, offering the precision required for engineering applications while keeping computational costs manageable. RANS relies on advanced turbulence modeling theories to close the equations, and numerous turbulence model theories and their modified versions have been proposed. For subsonic and supersonic flow in nozzles, accurate predictions are challenging for most turbulence models. To enhance the accuracy of turbulence numerical simulations, in this study, we explored a novel turbulence model, namely the algebraic stress model k-kL-ARSM+J (Abdol-Hamid, 2019). This model was applied to perform numerical calculations of the performance of the 3D supersonic asymmetric truncated nozzle under off-design conditions, with the aim of providing realistic patterns of change. This study enhances the understanding of the performance of 3D asymmetric nozzles, providing valuable insights for the design of aircraft engines.

2 Design methodology

The design of the nozzle involves four key steps:

(1) Use the minimum length nozzle theory (Argrow and Emanuel, 1988) to design an axisymmetric nozzle.

(2) Use streamlined tracing techniques to obtain a 3D asymmetric nozzle based on the shape at the combustion chamber exit.

(3) Implement a nonlinear compression truncation method to shorten the length of the 3D asymmetric nozzle.

(4) Use the Kriging surrogate model and the non-dominated sorting genetic algorithm (NSGA2) for multi-objective optimization of the nozzle.

Since this paper does not delve into the detailed nozzle design, only a brief introduction to the design methodology is provided below. For specific design methods, please refer to Zhu et al. (2018).

Fig. 1 depicts the specific design process for a 3D supersonic asymmetric truncated nozzle. The process begins by establishing a baseline flow field, using the MOC and minimum length nozzle (MLN) methods to derive an axisymmetric minimum length nozzle. Subsequently, a pressure ratio (PR) (representing the ratio of nozzle exit pressure to external flow pressure) is specified. Once the gas within the nozzle reaches a certain pressure, truncation is carried out from the nozzle's rear end. Simultaneously, a nonlinear truncation method is applied to further reduce the nozzle's length. CFD simulations are then used to obtain the flow field of the truncated nozzle, which serves as the baseline. A closed curve is selected at a specific location away from the center at the inlet of the baseline flow field. Through the use of discrete points from this curve, streamlined tracing techniques are used to extract streamlines from the flow field. These streamlines are then subjected to surface fitting to create the modified 3D nozzle geometry. Throughout the design process, the primary objectives are to optimize the lift and thrust of the offset nozzle. The truncation process of the axisymmetric nozzle is optimized to generate a truncated offset supersonic nozzle. Note that boundary layer corrections are necessary due to the effects of the boundary layer on the wall surfaces.

3 Turbulence model validation

The commonly used CFD method is founded on the RANS equations, which encompass two main categories of physical models: Reynolds stress models and eddy viscosity models. However, RANS methods based on eddy viscosity models have various shortcomings due to the limitations of linear eddy viscosity models. For example, in these models, the Reynolds stress tensor is proportional to the strain rate tensor (implying isotropic Reynolds stresses), leading to significant deviations between predicted results and experimental data (Su and Yuan, 2017). Wilcox (1998) summarized some types of applications in which linear eddy viscosity models have failed and are noteworthy, including flows with sudden changes in mean strain rate, flows over curved surfaces, rotational flows (vortical flows), and 3D flows. Due to the inherent limitations of linear eddy viscosity models, many researchers have begun to investigate nonlinear eddy viscosity models and Reynolds stress models in pursuit of obtaining more accurate numerical simulation results.

3.1 *k-kL* turbulence model

The *k-kL* model is a linear turbulence model, and its constitutive relations are based on the Boussinesq hypothesis, expressed as follows:

$$\tau_{ij}=2\mu_{\mathrm{t}}\left(S_{ij}-\frac{1}{3}\mathrm{tr}\{\boldsymbol{S}\}\delta_{ij}\right)-\frac{2}{3}\rho k\delta_{ij}, \tag{1}$$

$$\frac{\partial\rho k}{\partial t}+\frac{\partial\rho u_j k}{\partial x_j}=P_k+\frac{\partial}{\partial x_j}\left((\mu+\sigma_k\mu_{\mathrm{t}})\frac{\partial\rho k}{\partial x_j}\right)-C_{\mathrm{w}}\mu\frac{k}{d^2}-C_k\rho\frac{k^{2.5}}{kL}, \tag{2}$$

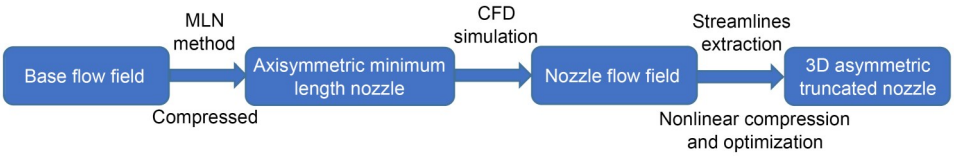

Fig. 1 Three-dimensional supersonic asymmetric truncated nozzle design process

$$\frac{\partial \rho kL}{\partial t}+\frac{\partial \rho u_j kL}{\partial x_j}=C_{kL}\frac{kL}{k}P_{kL}+\frac{\partial}{\partial x_j}\left((\mu+\sigma_{kL}\mu_t)\frac{\partial \rho kL}{\partial x_j}\right)-6\mu\frac{kL}{d^2}f_{kL}-C_{(kL)_2}\rho k^{1.5}, \tag{3}$$

where τ_{ij} is the component of the Reynolds stress tensor, μ_t is the turbulent eddy viscosity, S_{ij} is the component of the symmetric strain rate tensor $\boldsymbol{S}$, u_j is the velocity component in the j-direction, x_j is the coordinate in a specific direction, δ_{ij} is the Kronecker delta function, ρ is the density, k is the turbulent kinetic energy, t is the time, P_k is the production of turbulent kinetic energy, P_{kL} is the production of turbulent kL, L is the turbulent length scale, μ is the bulk viscosity, d is the distance normal to surface, σ_k, σ_{kL}, C_w, C_k, and $C_{(kL)_2}$ are constant coefficients, and f_{kL} and C_{kL} are the auxiliary functions in kL transport equation (Abdol-Hamid et al., 2016).

To streamline the content, please refer to Abdol-Hamid et al. (2016) for the specific parameters of the equations.

3.2 *k-kL*-ARSM+J nonlinear model

In addition to proposing the *k-kL* turbulence model with the eddy viscosity assumption, Abdol-Hamid (2019) introduced the *k-kL*-ARSM+J model, using an algebraic stress model to represent the Reynolds stress tensor. Their studies indicate that this model has the potential to improve the precision of numerical simulations, more closely mirroring the intricacies of turbulent motion, while maintaining computational resource requirements comparable to conventional two-equation turbulence models. The following introduces the algebraic stress model based on the *k-kL* model.

In the *k-kL*-ARSM+J model, the turbulent stress relationship is a blend between a linear model and an explicit algebraic stress relationship based on a three-basis approximation. Its stress constitutive relationship is as follows:

$$\tau_{ij}=f_2\tau_{ij}^{(\mathrm{ARSM})}+(1-f_2)\tau_{ij}^{(\mathrm{L})}, \tag{4}$$

where f_2 is the blending function for model corrections, similar to the one used by shear stress transport (SST) to switch between k-ω and k-ε. $\tau_{ij}^{(\mathrm{L})}$ represents the linear constitutive relationship for this model, and the algebraic stress relationship $\tau_{ij}^{(\mathrm{ARSM})}$ is expressed as:

$$\tau_{ij}^{(\mathrm{ARSM})}=-\rho k\left(\beta_1 T_{ij}^{(1)}+\beta_2 T_{ij}^{(2)}+\beta_4 T_{ij}^{(4)}+\frac{2}{3}\delta_{ij}\right), \tag{5}$$

$$T_{ij}^{(1)}=\left[S_{ij}^*-\frac{1}{3}\mathrm{tr}\{\boldsymbol{S}^*\}\right], \tag{6}$$

$$T_{ij}^{(2)}=\left[S_{ik}^*S_{kj}^*-\frac{1}{3}\mathrm{tr}\{\boldsymbol{S}^{*2}\}\right], \tag{7}$$

$$T_{ij}^{(4)}=[S_{ik}^*W_{kj}^*-W_{ik}^*S_{kj}^*], \tag{8}$$

where $T_{ij}^{(1)}$ represents the linear portion of this expression, while $T_{ij}^{(2)}$ and $T_{ij}^{(4)}$ correspond to the nonlinear terms used to simulate the anisotropy of Reynolds stresses. In the above equations,

$$S_{ij}^*=\tau S_{ij},\ W_{ij}^*=\tau W_{ij},$$
$$S_{ij}=\frac{1}{2}\left(\frac{\partial u_i}{\partial x_j}+\frac{\partial u_j}{\partial x_i}\right),\ W_{ij}=\frac{1}{2}\left(\frac{\partial u_i}{\partial x_j}-\frac{\partial u_j}{\partial x_i}\right),$$
$$\tau=\frac{C_\mu^{1/4}}{C_\mu}\frac{kL}{k^{3/2}},\ \beta_1=-2C_\mu^*=2\alpha,$$
$$\beta_2=-2a_4a_3\beta_1,\ \beta_4=a_4a_2\beta_1,$$

where τ, α, C_μ^*, and a_4 are variable coefficients, and a_2, a_3, and C_μ are constant coefficients. In this model, C_μ^* is constrained to be not less than 0.0005, and $C_\mu^*=-\alpha$ is obtained through the following cubic equation:

$$\alpha^3+p\alpha^2+q\alpha+r=0, \tag{9}$$

where p, q, and r are coefficients. The coefficients in the equations are:

$$a_1=\frac{1}{2}\left(\frac{4}{3}-C_2\right),\ a_2=\frac{1}{2}(2-C_4),\ a_3=\frac{1}{2}(2-C_3),$$
$$a_4=\left[\gamma_1^*-2\gamma_0^*(-C_\mu^*)\eta^2\tau^2\right]^{-1},\ \eta^2=\{S^2\}=S_{ij}S_{ij},$$
$$\gamma_0^*=\frac{C_1^1}{2},\ \gamma_1^*=\frac{1}{2}C_1^0+\left(\frac{C_{\varepsilon2}-C_{\varepsilon1}}{C_{\varepsilon1}-1}\right),\ r=\frac{\gamma_1^*a_1}{(2\eta^2\tau^2\gamma_0^*)^2},$$
$$p=-\frac{\gamma_1^*}{\eta^2\tau^2\gamma_0^*},\ R^2=-\frac{\{W^2\}}{\{S^2\}},\ \{W^2\}=-W_{ij}W_{ij},$$
$$q=\frac{1}{(2\eta^2\tau^2\gamma_0^*)^2}\left(\gamma_1^{*2}-2\eta^2\tau^2\gamma_0^*a_1-\frac{2}{3}\eta^2\tau^2a_3^2+2R^2\eta^2\tau^2a_2^2\right),$$
$$C_{\varepsilon1}=1.44,\ C_{\varepsilon2}=1.83,\ C_1^1=1.8,\ C_1^0=3.4,$$
$$C_2=0.36,\ C_3=1.25,\ C_4=0.6.$$

The correct root selected from this cubic equation should be the one with the smallest real part:

If $\eta^2\tau^2<1\times10^{-6}$, then $C_\mu^*=\dfrac{\gamma_1^* a_1}{\gamma_1^{*2}-2\{W^2\}\tau^2 a_2^2}$.

Otherwise, define

$$a=q-\frac{p^2}{3},\ b=\frac{1}{27}(2p^3-9pq+27r),\ d=\frac{b^2}{4}+\frac{a^3}{27}. \tag{10}$$

If $d>0$, then

$$\begin{aligned} &t_1=\left(-\frac{b}{2}+\sqrt{d}\right)^{1/3},\ t_2=\left(-\frac{b}{2}-\sqrt{d}\right)^{1/3},\\ &C_\mu^*=-\min\left(-\frac{p}{3}+t_1+t_2,\ -\frac{p}{3}-\frac{t_1}{2}-\frac{t_2}{2}\right). \end{aligned} \tag{11}$$

If $d\leqslant0$, then

$$\begin{aligned} &\theta=\cos^{-1}\left(-\frac{b/2}{\sqrt{-a^3/27}}\right),\ C_\mu^*=-\min(t_1,\ t_2,\ t_3),\\ &t_1=-\frac{p}{3}+2\sqrt{-\frac{a}{3}}\cos\left(\frac{\theta}{3}\right),\\ &t_2=-\frac{p}{3}+2\sqrt{-\frac{a}{3}}\cos\left(\frac{2\pi}{3}+\frac{\theta}{3}\right),\\ &t_3=-\frac{p}{3}+2\sqrt{-\frac{a}{3}}\cos\left(\frac{4\pi}{3}+\frac{\theta}{3}\right). \end{aligned} \tag{12}$$

In this algebraic stress model, the coefficients in Eqs. (2) and (3) are modified as follows:

$$\begin{aligned} &\sigma_k=f_2\sigma_{k1}+(1-f_2)\sigma_{k2},\\ &\sigma_{k1}=1.0,\ \sigma_{k2}=0.5,\ f_2=\tanh(\Gamma^2),\\ &\Gamma=\max\left(2\frac{\sqrt{k}}{C_\mu\omega d},\ \frac{500v}{d^2\omega}\right),\ \omega=\frac{k^{3/2}}{kLC_\mu^{1/4}}, \end{aligned} \tag{13}$$

$$\begin{aligned} &C_k=C_\mu^{3/4}(1+f_c),\ C_{(kL)_2}=\zeta_3+2.5C_\mu^{3/4}f_c,\\ &f_c=1.5(1.0-f_2)(M_t^2-M_0^2)H[M_t^2-M_0^2],\\ &M_t=\sqrt{\frac{2k}{a^2}},\ M_0=0.1, \end{aligned} \tag{14}$$

where v is the kinematic viscosity, ζ_3 is a constant coefficient with a value of 0.13, and $H[M_t^2-M_0^2]$ is the Heaviside function.

3.3 Verification

To verify the accuracy and effectiveness of this turbulence model in nozzle flow calculations, a National Aeronautics and Space Administration (NASA) standard case was selected as the validation case. The calculation accuracies of different turbulence models were compared. The experimental data referenced in this study were obtained from Seiner's experiment (Seiner et al., 1992).

The geometric model of the case is shown in Fig. 2. Given the difficulty of achieving flow convergence into quiescent air in this high-shear flow scenario, simulations were performed under background environmental conditions with an incoming flow of Ma_∞=0.01, where Ma_∞ is the incoming Mach number.

The inflow conditions used for the simulation were as follows: Ma_∞=0.01, T_∞=278 K, and Re_{D_jet}=22150, with inlet conditions of P_t/P_∞=7.824 and T_t/T_∞=1.127, where Re_{D_jet} is the unit Reynolds number, P_t/P_∞ is the ratio of total pressure to static pressure, and T_t/T_∞ is the ratio of total temperature to static temperature. The governing equations use the RANS method, and the low-diffusion flux-splitting scheme (LDFSS) is used for the inviscid flux term and the Vanalbada flux limiter. Three turbulence models, namely k-kL,

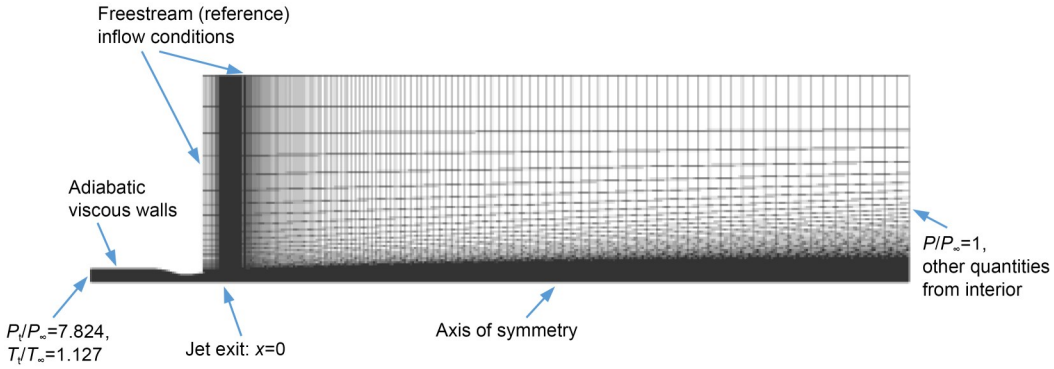

Fig. 2 Explanation of boundary conditions

k-*kL*-ARSM+J, and SST, were compared. Fig. 3 represents the grid independence verification for the case, using three sets of grids, namely Grid1 (3500), Grid2 (14000), and Grid3 (56000). The height of the first layer of these meshes ensures that y^+<1. The turbulence model used for the calculation was *k*-*kL*-ARSM+J. Fig. 3 shows that Grid2 was a suitable grid, and so for subsequent simulations, to balance computational cost and accuracy, Grid2 was chosen for numerical simulation.

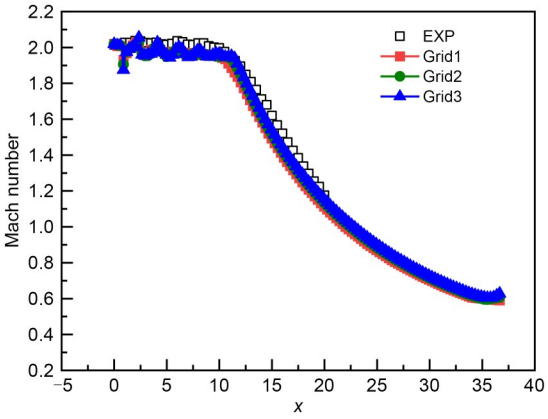

Fig. 3 Grid independence verification (EXP represents the experimental data)

Fig. 4 shows velocity distributions and Fig. 5 shows pressure distributions under different turbulence models. Fig. 4 shows that the numerical simulation results of the *k*-*kL*-ARSM+J model align most closely with the experimental data, accurately predicting the jet core region. In contrast, both the SST and *k*-*kL* models fail to correctly predict the jet core region, providing shorter predictions. Similar trends can be

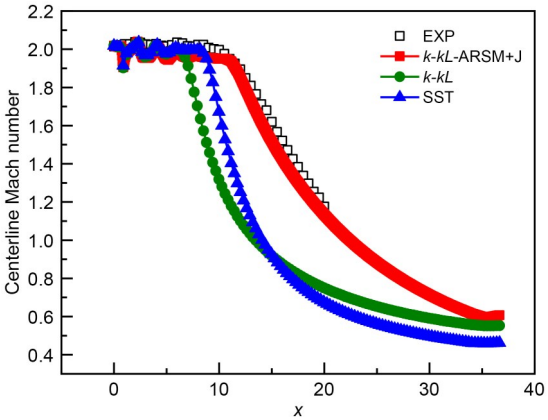

Fig. 4 Velocity distribution under different turbulence models

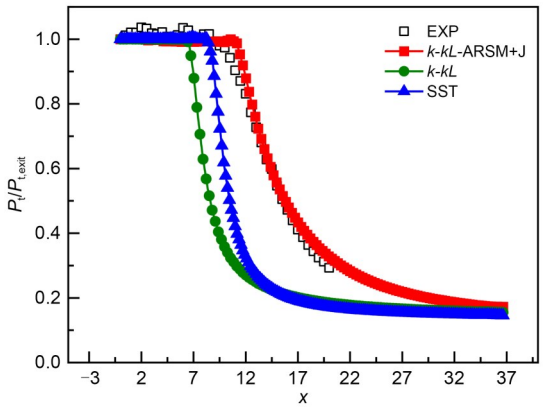

Fig. 5 Pressure distribution under different turbulence models ($P_{t,exit}$ is the total pressure at the exit)

observed in the axial pressure distributions depicted in Fig. 5.

The jet flow can be categorized into inner and outer boundaries, with the region between them known as the jet boundary layer. This boundary layer expands as the flow progresses in the *x*-direction, allowing more ambient medium to enter the boundary layer. As it progresses inward, it interacts with the region retaining the initial velocity (the jet core region), exchanging both momentum and mass, and gradually diminishing this region. Consequently, as the distance along the *x*-direction increases, the jet boundary layer widens. Further analysis, in combination with Fig. 6, reveals that both the SST and *k*-*kL* turbulence models

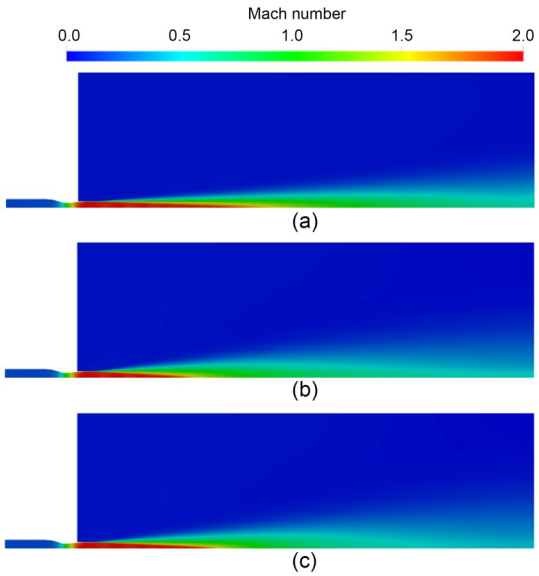

Fig. 6 Mach number contours under different turbulence models: (a) *k*-*kL*-ARSM+J; (b) *k*-*kL*; (c) SST. References to color refer to the online version of this figure

predict a shorter jet core region. This is due to an overestimation of the mixing rate at the inner boundary, resulting in an inaccurate estimation of momentum and mass exchange with the surrounding medium in the core region. Cloud maps indicate that these two turbulence models overestimate mixing rates in the main section, leading to a rapid decrease in Mach number in the center of the main section.

In summary, the *k*-*kL*-ARSM+J algebraic stress model provides more accurate predictions of the interaction between the inner and outer flows at the jet nozzle exit and allows for precise calculations of the jet nozzle's performance.

4 Numerical simulation of 3D supersonic asymmetric truncated nozzle

4.1 Numerical simulation analysis of the nozzle under design conditions

The designed and optimized 3D supersonic asymmetric truncated nozzle (Fig. 7) was computed using an in-house code developed in the laboratory. The calculation uses the previously validated algebraic stress model, the *k*-*kL*-ARSM+J turbulence model. To reduce computational time and cost, symmetric boundary conditions are used for the nozzle. The nozzle walls have been set to adiabatic and no-slip boundary conditions, while design parameters of the nozzle are outlined in Table 1. The calculations are performed by the RANS governing equation, which is discretized using the LDFSS scheme and Vanalbada flux limiter.

In this study, three sets of unstructured grids were designed for grid independence verification, with 1469487, 3638927, and 6103683 grid elements, respectively. The first layer grid height was set to 1×10^{-6} m, ensuring the y^+ value was less than 1. Fig. 8 shows the grid independence verification. The curves for medium and fine grids coincide, indicating that the medium grid meets the requirements for grid independence. Therefore, the computations in this study were conducted using the medium grid. Fig. 9 shows a schematic representation of the medium grid.

The numerical calculations were carried out using the parameters for the designed conditions outlined in Table 1. Fig. 10 presents the Mach number contour obtained from the calculations, clearly showing the expansion wave system in the flow field, as indicated by the dashed lines in the figure. Due to the mismatch in velocities between the external flow and the fluid ejected from the nozzle, the contact point between the

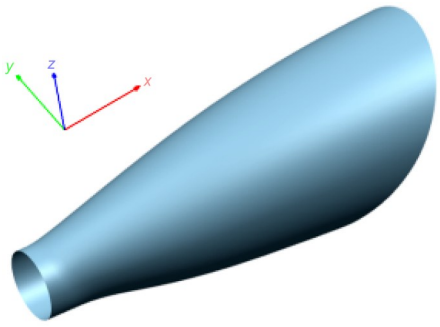

Fig. 7 Geometry of the nozzle

Table 1 Design parameters of the nozzle for the boundary conditions

Parameter	Value
Inlet pressure, P_{in} (Pa)	71700
Inlet Mach number	1.5
Inlet temperature (K)	2344
Far field pressure (Pa)	2511
Far field Mach number	5
Far field temperature (K)	221.65

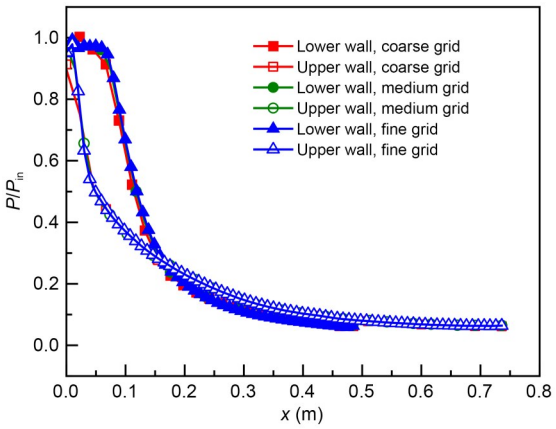

Fig. 8 Grid independence verification

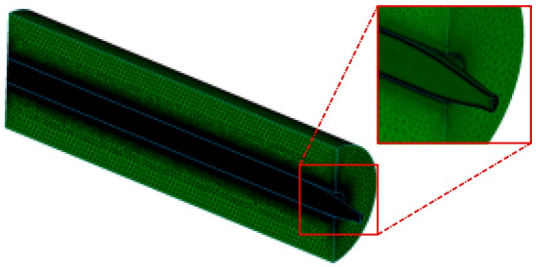

Fig. 9 Computational domain

external flow and the jet's outflow creates a viscous shear layer at the nozzle's trailing edge. Fig. 11 shows a comparison of the pressure distribution on the upper and lower walls of the nozzle's symmetric surface. The numerical simulation results align with the designed wall pressures, providing evidence that this computational approach is capable of accurately simulating the designed 3D supersonic nozzle.

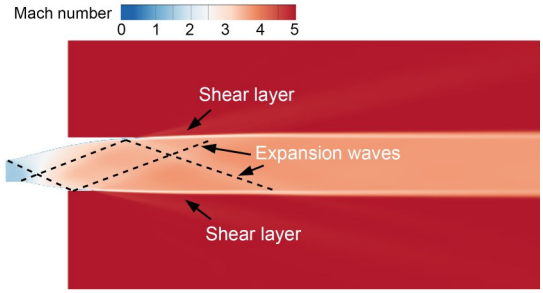

Fig. 10 Mach number contour for the designed conditions

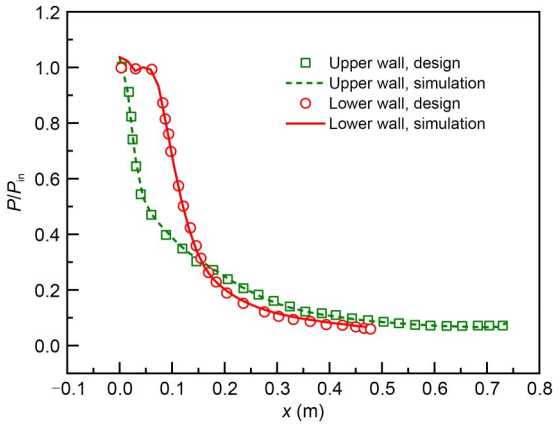

Fig. 11 Comparison of upper-wall and lower-wall pressures with design pressures

4.2 Numerical simulation analysis of the nozzle under off-design conditions

The results above show that the performance of the 3D supersonic asymmetric truncated nozzle under design conditions was accurately simulated and analyzed. However, in most cases, the nozzle operates under off-design conditions. To investigate the performance of the nozzle under off-design conditions, we considered variations in inlet velocity, inlet pressure, and operation height. The aim was to comprehensively understand the behavior of the designed nozzle under various off-design conditions. Some aerodynamic performance parameters, including thrust, lift, and pitch moment, were introduced to quantify the performance of the afterburner nozzle of a supersonic engine under different operating conditions. The reference point of the pitching moment was the center of the nozzle entrance. Thrust and lift were obtained by integrating the pressure difference and viscous drag on the entire numerical model's surfaces in the x and z directions, respectively. The formulas were as follows:

$$F_{\text{thrust}}=\int(p_{\text{w}}-p_{\text{amb}}-\boldsymbol{\tau}_{\text{w}}\cdot\boldsymbol{n}_x)\,\mathrm{d}s_1, \tag{15}$$

$$F_{\text{lift}}=\int(p_{\text{w}}-p_{\text{amb}})(\mathrm{d}s_2^{\text{upper}}-\mathrm{d}s_2^{\text{lower}})+\int(\boldsymbol{\tau}_{\text{w}}\cdot\boldsymbol{n}_z)\,\mathrm{d}s_2, \tag{16}$$

where F_{thrust} is the thrust, F_{lift} is the lift, p_{w} is the wall pressure, p_{amb} is the atmospheric pressure, $\boldsymbol{\tau}_{\text{w}}$ is the wall shear stress, s_1 represents the projected area of the nozzle surface on the yoz plane, and s_2 represents the projected area of the nozzle surface on the xoy plane. $\boldsymbol{n}_x$ and $\boldsymbol{n}_z$ correspond to the unit orthogonal vectors.

4.2.1 Influence of inlet parameters on nozzle performance

The inlet parameters of the nozzle are contingent upon the performance of the scramjet engine's inlet and combustion chamber. When these components operate under unstable conditions, the inlet parameters of the nozzle undergo significant variations. To investigate the effect of changes in inlet parameters on the nozzle's performance, we focused on the variations in inlet velocity and inlet pressure.

4.2.1.1 Effect of inlet velocity

In this section, we explore the influence of the inlet Mach number (Ma_{in}) on the nozzle's performance. The inlet Mach numbers selected were 1.0, 1.2, 1.4, 1.6, 1.8, and 2.0, with other boundary conditions set according to Table 1, and numerical simulations conducted for each case. Figs. 12 and 13 depict the variation of the thrust coefficient, lift, and pitching moment for the nozzle with changing inlet Mach numbers. Analysis shows that as the inlet Mach number increases, there is a corresponding increase in thrust coefficient. Notably, the maximum increase observed is 55.68% compared to the thrust coefficient at Ma_{in}= 1.0. However, lift initially increases with the inlet Mach number, reaching its peak at Ma_{in}=1.4, and then decreases. Thrust coefficient experiences a significant

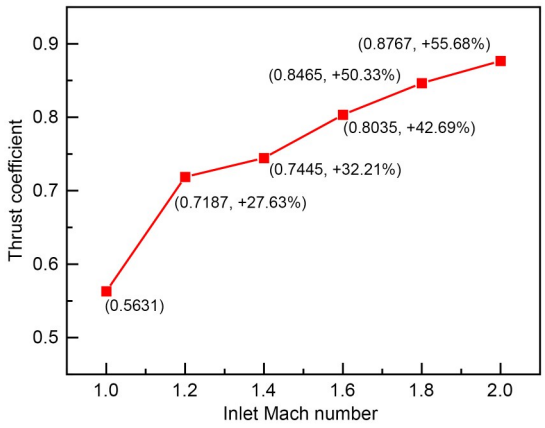

Fig. 12 Variation of thrust coefficient with inlet Mach number

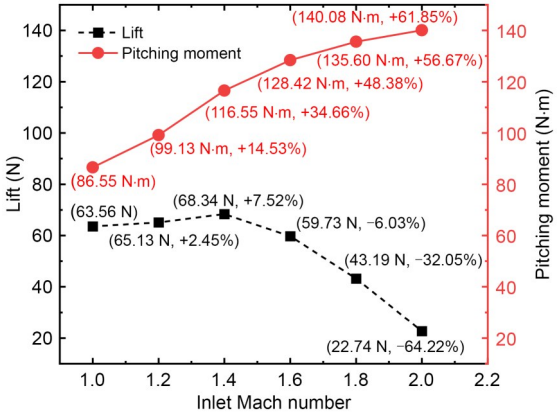

Fig. 13 Variation of lift and pitching moment with inlet Mach number

increase as the inlet Mach number increases from Ma_{in}= 1.0 to 1.2. To explore this phenomenon, Mach number contours were generated (Fig. 14). At an inlet Mach number of 1.0, there was a thick boundary layer along the nozzle wall. This occurs because when the inlet Mach number is at the critical Mach number of 1.0, there is still a local subsonic region near the inlet wall, resulting in a thicker boundary layer and consequently a smaller core nozzle area, which limits gas expansion and thus reduces thrust. However, as the inlet Mach number increases to 1.2, the entire inlet region transitions to supersonic flow, leading to a significant increase in thrust. Additionally, the velocity contours within the flow field become more symmetric with increasing inlet velocity. Consequently, the pressure difference between the upper and lower walls of the nozzle decreases, resulting in an initial increase followed by a decrease in lift. Fig. 14 reveals that with increasing inlet velocity, compression waves form

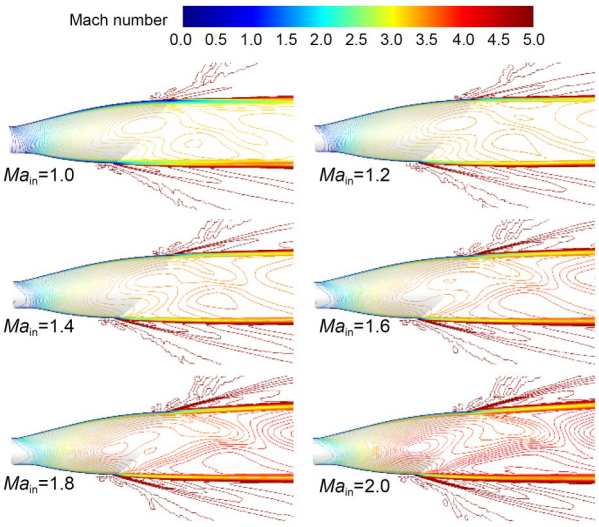

Fig. 14 Mach number contours on the symmetric plane for different inlet Mach numbers

near the lower wall of the nozzle. This is attributed to the nozzle's nonlinear truncation and biased design, resulting in a longer upper wall with a smoother profile and a shorter lower wall with a more abrupt profile. Therefore, as the flow expands in the nozzle's expansion region and undergoes redirection, it encounters more abrupt changes near the lower wall, leading to the formation of compression waves, particularly as the inlet Mach number increases.

For a more in-depth examination of the changes in the flow field with variable inlet Mach numbers, contours of the flow field were generated for each Mach number. Fig. 15 reveals that, with an increase in the inlet Mach number, the core region expands and the uniform region shifts backward. This leads to an overall increase in high-pressure regions (>5 kPa) within the nozzle, resulting in a greater net force from the gas pressure inside the nozzle and an increase in thrust. The contour lines in the figure show that the pressure increase on the lower wall of the nozzle is faster than that on the upper wall (this is due to the presence of compression waves). This difference in pressure growth causes an initial increase in lift, reaching its maximum value at a Mach number of 1.4, followed by a decrease. As the uniform region shifts backward, the point at which the lift force is applied by the nozzle also moves backward. Consequently, this leads to a continuous increment in the pitching moment of the nozzle. The backward movement of the uniform region also leads to incomplete expansion, resulting in higher exit pressures. To match

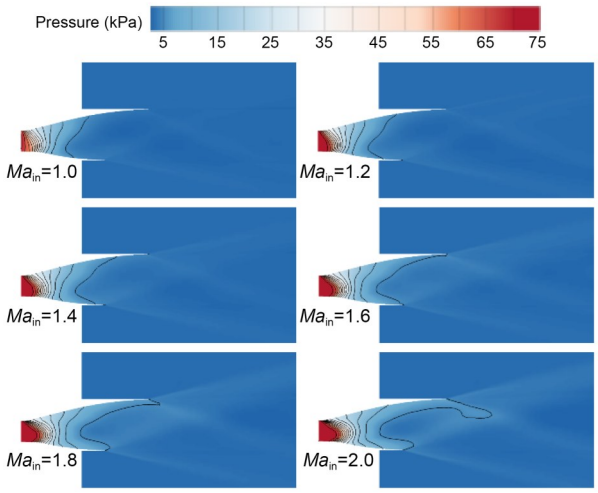

Fig. 15 Pressure contours on the symmetric plane for different inlet Mach numbers

the external flow pressure, the strength of the expansion wave system increases, which is more evident in the contours.

4.2.1.2 Effect of inlet pressure

The inlet pressure of the nozzle also has a crucial impact on its performance. To investigate the effect of variable inlet pressure on the designed nozzle, five different inlet pressures were chosen for numerical simulations: 50, 60, 70, 80, and 90 kPa. The other boundary conditions for the calculations are shown in Table 1. Fig. 16 shows the variation of the thrust coefficient with changing inlet pressure, while Fig. 17 shows the variation of lift and pitching moment with changing inlet pressure. The figures show that as the inlet pressure changes, the thrust coefficient, lift, and pitching moment all increase approximately in proportion. With every 10 kPa increase in inlet pressure, the

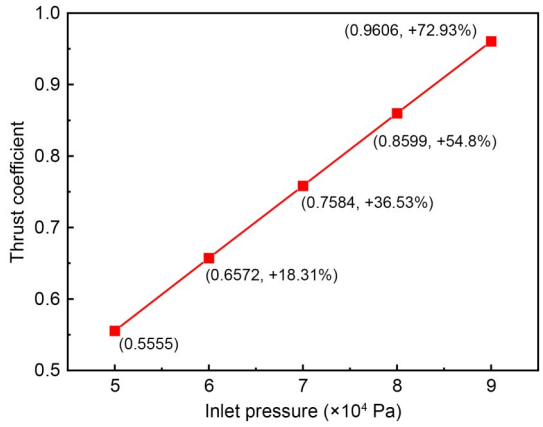

Fig. 16 Variation of thrust coefficient with inlet pressure

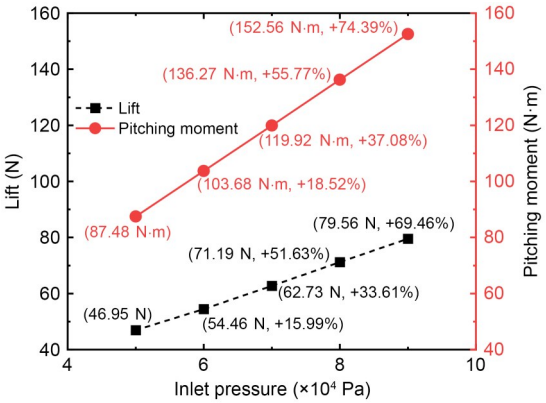

Fig. 17 Variation of lift and pitching moment with inlet pressure

total thrust coefficient increases by about 18.3%, lift increases by about 17.3%, and the pitching moment increases by about 18.5%.

When the airflow enters the nozzle, it expands, leading to an increase in velocity and a gradual decrease in pressure as the flow progresses. Fig. 18 shows the distribution of velocity contours on the symmetric plane of the nozzle. According to the Prandtl-Meyer flow relationship (Eq. (17)), when the airflow passes through an external corner, expansion waves are generated.

$$\theta=\vartheta(Ma_1)-\vartheta(Ma_2), \tag{17}$$

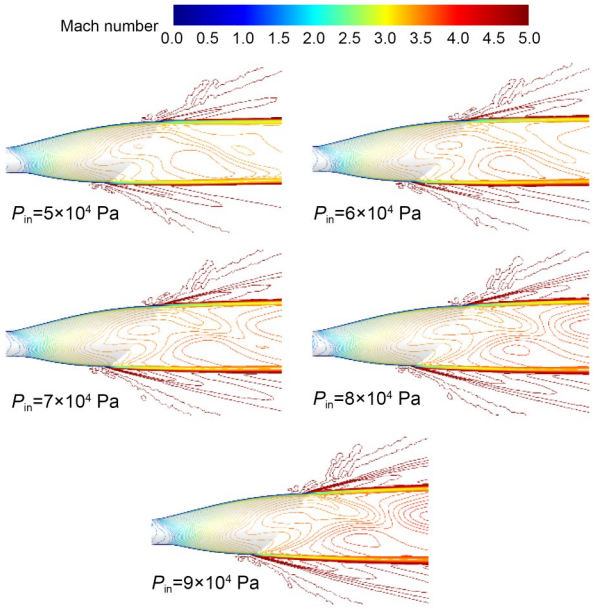

Fig. 18 Mach number contours on the symmetric plane for different inlet pressures (P_{in})

where θ is the external corner, and ϑ is a function of Mach number. The Mach number after the expansion wave (Ma_2) depends only on the upstream Mach number (Ma_1) and the magnitude of the external corner. Therefore, when the upstream Mach number remains constant, the Mach number distribution after passing through the expansion wave remains unchanged. Consequently, the Mach number distributions for the five cases shown in the figure are consistent. Thus, at this point, the ratio of pressure inside the nozzle after expansion to the inlet pressure is determined. The forces acting on the nozzle originate from the pressure exerted by the gas on the nozzle wall after expansion, resulting in a net force. Therefore, as the inlet pressure increases in proportion, the thrust coefficient, lift, and pitching moment of the nozzle also increase linearly in proportion.

To analyze the change in gas pressure within the nozzle resulting from the variation in inlet pressure, pressure contours inside the flow field were created (Fig. 19). With an increase in inlet pressure, the expansion of gas inside the nozzle intensifies, and the pressure exerted on the nozzle walls after expansion increases. Consequently, the nozzle provides more thrust as a result of the increased inlet pressure. The rate of pressure increase on the upper and lower walls of the nozzle is not consistent with the increase in inlet pressure. The increase in pressure on the upper wall is greater than that on the lower wall, resulting in an overall increase in lift. Apart from the increase in lift, the point of action of the lift force shifts backward. Therefore, the rate of increase in pitching moment is greater than that of lift.

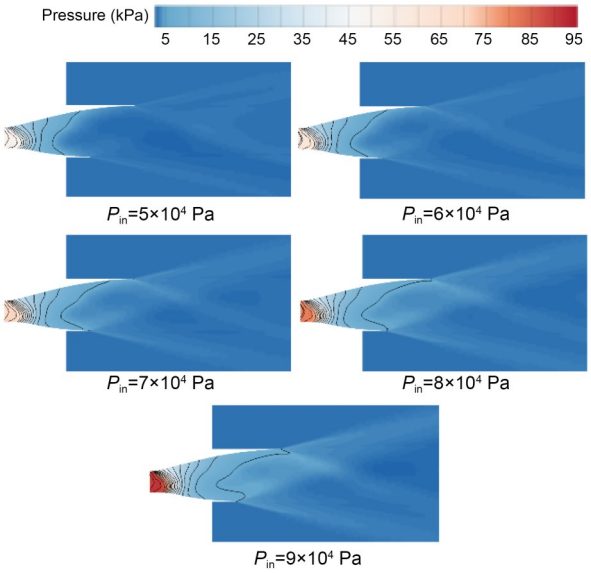

Fig. 19 Pressure contours on the symmetric plane for different inlet pressures

4.2.2 Influence of external flow parameters on nozzle performance

At hypersonic speeds, there are rapid changes in flight altitude. To gain a more comprehensive understanding of the impact of flight altitude on the designed nozzle, we considered five different flight altitudes, namely 20000, 22500, 25000, 27500, and 30000 m. The external flow parameters corresponding to these five flight altitudes are shown in Table 2. The other boundary conditions were the same as those in Table 1.

Table 2 Atmospheric parameters at different altitudes

Altitude (m)	Pressure (Pa)	Temperature (K)
20000	5474.89	216.65
22500	3699.54	219.15
25000	2511.02	221.65
27500	1711.75	224.15
30000	1171.87	226.65

Table 2 reveals that the atmospheric pressure values vary significantly with changes in flight altitude. Atmospheric pressure decreases rapidly with an increase in flight altitude, while temperature changes only slightly and gradually increases. The rapid changes in flight altitude lead to significant alterations in the flow field structure after the flow exits the nozzle. Fig. 20

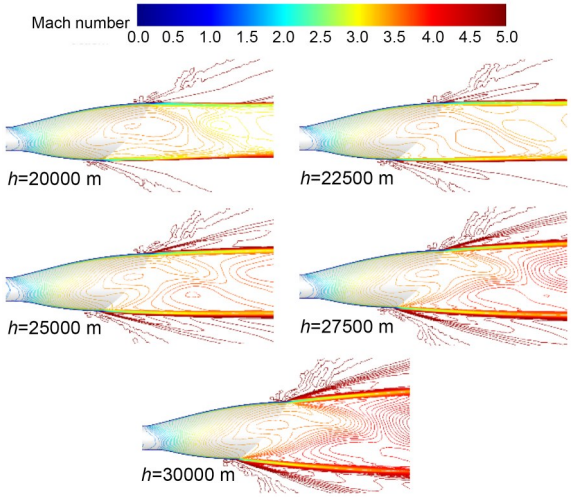

Fig. 20 Mach number contours on the symmetric plane at various flight altitudes (h)

shows Mach number contours within the symmetric plane of the nozzle at different flight altitudes. When the flight altitude is lower than the design altitude, such as 20 km, the far-field pressure is higher than the nozzle exit pressure. For these over-expanded flows, the shear layer converges towards the center of the nozzle. As the flight altitude increases, the far-field pressure decreases, and the flow field near the nozzle exit becomes under-expanded. The shear layers in these cases are horizontal or divergent, with divergent shear layers causing increased interference with the external flow. Consequently, as the altitude increases, the shock waves generated by the external flow become stronger.

Figs. 21 and 22 present thrust coefficient, lift, and pitching moment curves for the nozzle at different altitudes. With increasing altitude, the changes in thrust coefficient, lift, and pitching moment of the nozzle are relatively small: the maximum variation is 2.72% in the thrust coefficient, 8.05% in the lift, and 4.32% in the pitching moment. Fig. 23 also reveals that, at the five different flight altitudes, the pressure distributions on the symmetric plane of the nozzle are generally consistent. This indicates that changes in altitude have a limited impact on the nozzle's performance. This is because the supersonic upstream flow inside the nozzle influences the downstream flow. As a result, variations in external flow pressure and temperature have little influence on the internal flow field of the nozzle, leading to minor changes in nozzle performance parameters. Small performance changes originate from alterations in the boundary layer. Changes in external flow pressure significantly affect the adverse pressure gradient within the boundary layer, which, in turn, impacts boundary layer thickness, resulting in subtle variations in forces.

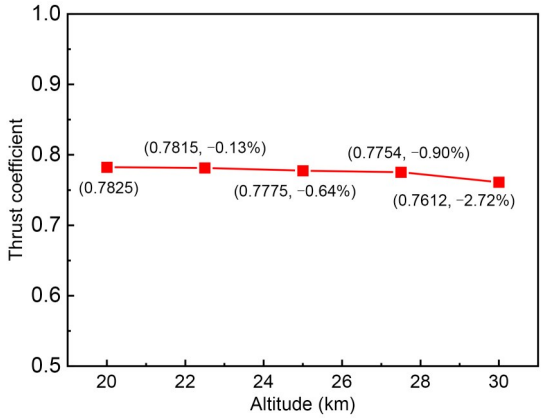

Fig. 21 Variation of the thrust coefficient with flight altitudes

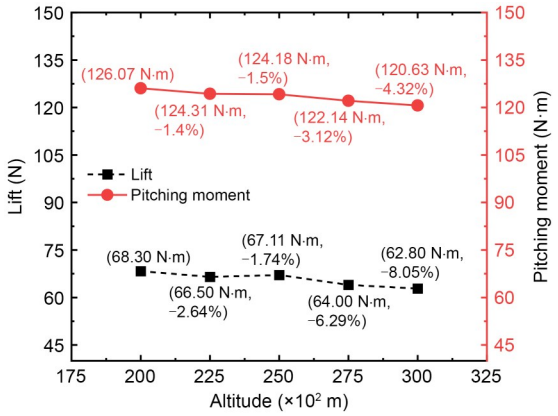

Fig. 22 Variation of the lift and pitching moment with flight altitudes

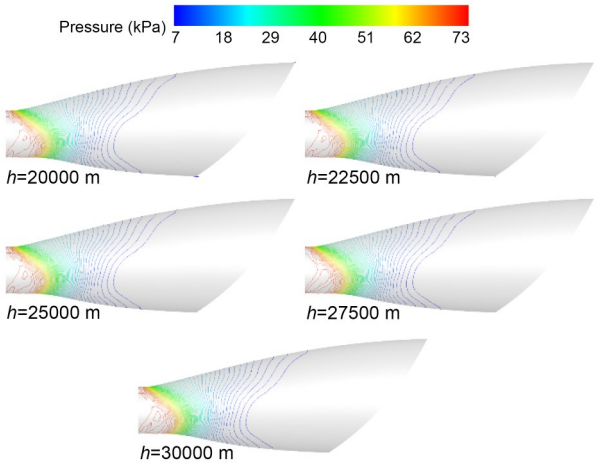

Fig. 23 Pressure contours on the symmetric plane of the nozzle at various flight altitudes

5 Conclusions

The object of this study was to numerically simulate a 3D supersonic asymmetric truncated nozzle, which was designed using the MLN design method, a nonlinear truncation method, and an optimization approach based on surrogate models. The study used the latest *k-kL* correction model to analyze the nozzle's performance under both design and off-design conditions. Off-design conditions included variations in inlet Mach number, inlet pressure, and flight altitude, with results and trends in nozzle performance obtained

under these conditions. The following conclusions can be drawn from this study:

(1) The NASA standard test cases showed that the *k-kL*-ARSM+J algebraic stress model provides accurate simulations of supersonic nozzles, closely matching experimental data. This model enables precise calculations of nozzle performance.

(2) With increasing inflow Mach number, the thrust and pitching moment increase while the rate of increase decreases. The lift reaches its peak near the design Mach number and then decreases rapidly. As inlet pressure increases, the nozzle thrust, lift, and pitching moment all show linear growth.

(3) With increasing flight altitude, the internal flow field of the nozzle remains essentially the same due to the consistent supersonic nozzle inlet conditions. However, external to the nozzle, changes in external flow pressure cause the nozzle exit to transition from over-expansion to under-expansion. As a result, the shear layer behind the nozzle first converges towards the center of the nozzle and then diverges.

Acknowledgments

This work is supported by the Zhejiang Provincial Key Research and Development Program of China (No. 2020C01020).

Author contributions

Gang WANG wrote the first draft of the manuscript. Gang WANG and Shuai ZHANG finished the numerical simulation. Jifa ZHANG and Yao ZHENG helped to organize the manuscript. Gang WANG and Jifa ZHANG revised and edited the final version.

Conflict of interest

Gang WANG, Shuai ZHANG, Jifa ZHANG, and Yao ZHENG declare that they have no conflict of interest.

References

Abdol-Hamid KS, 2019. Development of *kL*-based linear, nonlinear, and full Reynolds stress turbulence models. AIAA Scitech 2019 Forum. https://doi.org/10.2514/6.2019-1878

Abdol-Hamid KS, Carlson JR, Rumsey CL, 2016. Verification and validation of the *k-kL* turbulence model in FUN3D and CFL3D codes. The 46th AIAA Fluid Dynamics Conference. https://doi.org/10.2514/6.2016-3941

Argrow BM, Emanuel G, 1988. Comparison of minimum length nozzles. *Journal of Fluids Engineering*, 110(3): 283-288. https://doi.org/10.1115/1.3243546

Baysal O, 1992. Flow Analysis and Design Optimization Methods for Nozzle Afterbody of a Hypersonic Vehicle. NASA Contractor Report No. 4431, Langley Research Center, NASA, Washington, USA.

Billig FS, Kothari AP, 2000. Streamline tracing: technique for designing hypersonic vehicles. *Journal of Propulsion and Power*, 16(3):465-471. https://doi.org/10.2514/2.5591

Edwards C, Small W, Weidner J, et al., 1975. Studies of scramjet/airframe integration techniques for hypersonic aircraft. The 13th Aerospace Sciences Meeting. https://doi.org/10.2514/6.1975-58

Göing M, 1990. Nozzle design optimization by method-of-characteristics. The 26th Joint Propulsion Conference. https://doi.org/10.2514/6.1990-2024

Gruhn P, Henckels A, Kirschstein S, 2000. Flap contour optimization for highly integrated SERN nozzles. *Aerospace Science and Technology*, 4(8):555-565. https://doi.org/10.1016/S1270-9638(00)01080-4

Gruhn P, Henckels A, Sieberger G, 2002. Improvement of the SERN nozzle performance by aerodynamic flap design. *Aerospace Science and Technology*, 6(6):395-405. https://doi.org/10.1016/S1270-9638(02)01177-X

Herrmann H, Rick H, 1991. Propulsion aspects of hypersonic turbo-ramjet-engines with special emphasis on nozzle/aftbody integration. ASME International Gas Turbine and Aeroengine Congress and Exposition, article V002T02A039. https://doi.org/10.1115/91-GT-395

Hirschen C, Gülhan A, 2009. Infrared thermography and pitot pressure measurements of a scramjet nozzle flowfield. *Journal of Propulsion and Power*, 25(5):1108-1120. https://doi.org/10.2514/1.41787

Hirschen C, Gülhan A, Beck WH, et al., 2008. Experimental study of a scramjet nozzle flow using the pressure-sensitive-paint method. *Journal of Propulsion and Power*, 24(4):662-672. https://doi.org/10.2514/1.34626

Hirschen C, Gülhan A, Beck WH, et al., 2009. Measurement of flow properties and thrust on scramjet nozzle using pressure-sensitive paint. *Journal of Propulsion and Power*, 25(2):267-280. https://doi.org/10.2514/1.37957

Koschel W, Rick W, 1991. Design considerations for nozzles of hypersonic airbreathing propulsion. The 3rd International Aerospace Planes Conference. https://doi.org/10.2514/6.1991-5019

Lederer R, Krüger W, 1993. Nozzle development as a key element for hypersonics. The 5th International Aerospace Planes and Hypersonics Technologies Conference. https://doi.org/10.2514/6.1993-5058

Li R, Xu JL, Yu KK, et al., 2021. Design and analysis of the scramjet nozzle with contact discontinuity. *Aerospace Science and Technology*, 113:106695. https://doi.org/10.1016/j.ast.2021.106695

Liao L, Yan L, Huang W, et al., 2018. Mode transition process in a typical strut-based scramjet combustor based on a parametric study. *Journal of Zhejiang University-SCIENCE A (Applied Physics & Engineering)*, 19(6): 431-451.

https://doi.org/10.1631/jzus.A1700617

Lv Z, Xia ZX, Liu B, et al., 2017. Preliminary experimental study on solid-fuel rocket scramjet combustor. *Journal of Zhejiang University-SCIENCE A (Applied Physics & Engineering)*, 18(2):106-112. https://doi.org/10.1631/jzus.A1600489

Miao JJ, Cai YW, Wang D, et al., 2023. Optimum design method oriented thrust for over-under TBCC combined nozzle. *Journal of Aerospace Power*, 38(6):1367-1377 (in Chinese). https://doi.org/10.13224/j.cnki.jasp.20220883

Nickerson G, Dunn S, Migdal D, 1988. Optimized supersonic exhaust nozzles for hypersonic propulsion. The 24th Joint Propulsion Conference. https://doi.org/10.2514/6.1988-3161

Quan ZB, Xu JL, Mo JW, 2012. Design of nonlinearly compressed SERN profile. *Journal of Propulsion Technology*, 33(6):951-955 (in Chinese). https://doi.org/10.13675/j.cnki.tjjs.2012.06.010

Seiner JM, Ponton MK, Jansen BJ, et al., 1992. The effects of temperature on supersonic jet noise emission. The 14th DGLR/AIAA Aeroacoustics Conference, p.295-307.

Su XR, Yuan X, 2017. Improved compressor corner separation prediction using the quadratic constitutive relation. *Proceedings of the Institution of Mechanical Engineers, Part A: Journal of Power and Energy*, 231(7):618-630. https://doi.org/10.1177/0957650917709367

Wang SY, Fu X, Yang XL, et al., 2021. Progresses and challenges of high-order-moment turbulence closure. *Advances in Mechanics*, 51(1):29-61 (in Chinese). https://doi.org/10.6052/1000-0992-20-029

Wen X, Liu J, Li J, et al., 2019. Design and numerical simulation of a clamshell-shaped inlet cover for air-breathing hypersonic vehicles. *Journal of Zhejiang University-SCIENCE A (Applied Physics & Engineering)*, 20(5):347-357. https://doi.org/10.1631/jzus.A1800620

Wilcox DC, 1998. Turbulence Modeling for CFD. 2nd Edition. DCW Industries, La Cãnada, USA.

Yu HX, Wei ZJ, 2023. Experimental and numerical investigation on design parameters of slot nozzles. *Aerospace Science and Technology*, 141:108509. https://doi.org/10.1016/j.ast.2023.108509

Yu KK, Chen YL, Huang S, et al., 2020. Inverse design method on scramjet nozzles based on maximum thrust theory. *Acta Astronautica*, 166:162-171. https://doi.org/10.1016/j.actaastro.2019.10.024

Zhang WH, Liu J, Ding F, et al., 2019. Novel integration methodology for an inward turning waverider forebody/inlet. *Journal of Zhejiang University-SCIENCE A (Applied Physics & Engineering)*, 20(12):918-926. https://doi.org/10.1631/jzus.A1900334

Zheng JL, Chang JT, Yang SB, et al., 2019. Trajectory optimization for a TBCC-powered supersonic vehicle with transition thrust pinch. *Aerospace Science and Technology*, 84:214-222. https://doi.org/10.1016/j.ast.2018.10.026

Zhu MJ, Fu L, Zhang S, et al., 2018. Design and optimization of three-dimensional supersonic asymmetric truncated nozzle. *Proceedings of the Institution of Mechanical Engineers, Part G: Journal of Aerospace Engineering*, 232(15):2923-2935. https://doi.org/10.1177/0954410017718567